



**HAL**  
open science

## Steady rotation of a Mach shock: experimental and numerical evidences

Vincent Rodriguez, J. Melguizo-Gavilanes, Vianney Monnier, Pierre Vidal,  
Ratiba Zitoun

► **To cite this version:**

Vincent Rodriguez, J. Melguizo-Gavilanes, Vianney Monnier, Pierre Vidal, Ratiba Zitoun. Steady rotation of a Mach shock: experimental and numerical evidences. Experiments in Fluids, 2023, 10.1007/s00348-023-03612-z . hal-03867085v2

**HAL Id: hal-03867085**

**<https://hal.science/hal-03867085v2>**

Submitted on 22 Nov 2023

**HAL** is a multi-disciplinary open access archive for the deposit and dissemination of scientific research documents, whether they are published or not. The documents may come from teaching and research institutions in France or abroad, or from public or private research centers.

L'archive ouverte pluridisciplinaire **HAL**, est destinée au dépôt et à la diffusion de documents scientifiques de niveau recherche, publiés ou non, émanant des établissements d'enseignement et de recherche français ou étrangers, des laboratoires publics ou privés.

# Steady rotation of a Mach shock: experimental and numerical evidences

V. Rodriguez · J. Melguizo-Gavilanes · V. Monnier · P. Vidal · R. Zitoun

Revised: 25 January 2023 / Accepted: 22 February 2023, Experiments in Fluids

**Abstract** This experimental and numerical work reports on the dynamical behaviour of a shock in an inert gas at the concave wall of a hollow circular chamber. The gas in the chamber was air or  $\text{He} + \text{O}_2 + 2 \text{Ar}$  at initial pressures  $p_{c0}$  ranging from 2 to 12 kPa and initial temperature  $T_0 = 288$  K. The shock was generated using a detonation driven shock tube. The shock dynamics were characterized through high-speed shadowgraph recordings and high-resolution numerical simulations. For each gas and  $p_{c0}$ , the experiments evidenced the formation of a Mach reflection along the wall and identified a range of initial pressures for which this configuration rotates with constant stem heights and constant velocities larger than those at the chamber entry. The numerical simulations were capable of capturing the dynamics quantitatively. These results extend to inert gases our previous work with a reactive gas for which we reported on the possibility of a steadily rotating overdriven Mach detonation. The steadiness range is narrower with the inert gases, likely because of the smaller initial pressure ratios at the chamber entry and lower support from the subsonic flow behind the shock. The initial support in the reactive case was more efficient because the discontinuities at the chamber entry were self-sustained Chapman-Jouguet detonations. Further investigations of these Mach rotating regimes should rely only on specific experiments and numerical simulations, for example, on the effect of the chamber dimensions, because of the complex non-dimensional formulation of the problem.

**Keywords** shock dynamics · Mach reflection · high-speed visualization · OpenFOAM simulation

## 1 Introduction

Shock and detonation dynamics in curved confinements is a fundamental topic in compressible hydrodynamics because of the variety and complexity of wave interactions and behaviours that such boundaries can generate. This includes oblique shock reflection and diffraction, Mach stems and fresh-burnt gases interfaces and their instabilities. Their modelling is most often out of reach of theoretical developments and their numerical simulation also remains a numerical challenge, in particular for reactive media.

Applications include defence (e.g., shock wave shaping), safety (e.g., core envelope in nuclear power plants) and advanced propulsion. In particular, detonation is currently considered an alternative to isobaric combustion usually utilized in turboprops. Combustion chambers in rotating detonation engines (RDE) can be annular [1–4], hollow [5,6], or semi-hollow [7–10]; the latter two appear to produce the higher pressures and wave rotation velocities.

A review of experimental and numerical work on detonation in converging curved channels and chambers [11–19] can be found in [20,21]. The main effect of such confinements is to increase the component of the wavefront velocity tangent to the outer wall. Indeed, in the reference frame attached to the front, the situation is similar to that of a converging shock. The dynamical behaviour, however, strongly depends on the set-up geometry. The consequence of edge effects at walls may also differ significantly depending on whether the reactive medium is initially gaseous or solid. In gases, they

---

V. Rodriguez · J. Melguizo-Gavilanes · V. Monnier · P. Vidal · R. Zitoun  
Institut Pprime, UPR 3346, Fluid, Thermal, and Combustion  
Department, ISAE-ENSMA, BP 40109, 86960 Futuroscope-  
Chasseneuil, France  
E-mail: vincent.rodriguez@ensma.fr

appear as successive quenching and re-ignitions as the radius decreases, and too small radii result in complete quenching.

For a curved, constant cross-section channel, the larger its radius of curvature, the closer the detonation to the planar, ideal Chapman-Jouguet (CJ) detonation. The criterion for quasi-CJ propagation is that the radius should be at least 23 times the average width of cells that structure the detonation reaction zone of the reactive mixture considered [14,15]. For the hollow chamber, that is, without an inner wall, our group recently reported the existence of a steadily-rotating Mach detonation front. Its properties are a front normal to the wall, with velocity component tangent to the chamber outer wall higher than the CJ velocity, and with cells significantly smaller than the chamber radius and those present in a CJ wave, that keep parallel to the propagation direction of the front (i.e., the local tangent to the wall). The latter outcome suggests that chemical kinetics, which determines the cellular structure, is not the controlling factor for observing this regime of rotating overdriven Mach detonations. First, its cell widths are too small to be a relevant characteristic length, and, second, its global dynamical behaviour is reproduced correctly through numerical modelling based on Whitham's Geometrical Shock Dynamics [22,23], i.e., on an evolution equation for the front shape and position without other characteristic length than those defined by the boundary conditions. Consequently, this regime is driven only by the curvature of the chamber wall and the front initial velocity at the curved chamber entry. In our conditions, the CJ regime, whose velocity is essentially determined by the heat of reaction of the reactive mixture.

This Mach detonation is a particular example of the two classical dynamical configurations observed when a discontinuity becomes oblique to a wall, e.g., [24,25]. The regular reflection shows two shock-type discontinuities attached to the same moving point along the wall, one incident at an acute angle relative to the propagation direction and the other reflected at an obtuse angle relative to this direction. The irregular - or Mach - reflection shows four waves. One is the Mach stem (i.e. a shock-type discontinuity normal to the wall), two are shock-type discontinuities that form the same acute-obtuse pattern as in the regular reflection but with their attachment point on the Mach stem, at some distance from the wall, and one is a contact-type discontinuity - a slip line - attached to the former two on the Mach stem, below the obtuse-angle reflected shock. Depending on the conditions, the Mach reflection can be steady, that is, the distance of its triple-shock point to the wall

is constant. This is the case in our former and present analyses.

This article thus reports on a continuation with inert gases of our investigation with reactive gases summarized above. The incident front is a shock, not a detonation, since there is no heat of reaction to determine its initial velocity, and, of course, there is no cellular instability. The results provide experimental and numerical evidence that a steadily-rotating Mach front can also be generated. Section 2 and 3 describe the experimental setup and methodology, and the numerical procedure, respectively. Sections 4 and 5 detail the experimental results and compares them against numerical simulations. Finally, Section 6 discusses and concludes this work.

## 2 Setup and experimental methodology

Figure 1 shows the schematic of the setup. The main three elements are the curved chamber (80 mm outer-wall radius  $R_{out}$ , 30 mm inner-wall radius  $R_{in}$  centered 20 mm from that of the outer radius, closer to the chamber entry), the tube (2 m long, 51 mm inner diameter) that drives the initial discontinuity into the chamber, and the expansion vessel at the chamber exit. An 18  $\mu\text{m}$  thick Mylar foil separated the tube and the chamber and another one the chamber and the vessel. After vacuuming the tube and the curved chamber, the tube was filled up with a premixed reactive gas and the chamber with an inert gas. The setup is thus a detonation-driven shock tube. A deflagration was ignited at one end of the tube, and its transition to detonation was promoted using the classical Shchelkin spiral technique. The detonation interaction with the Mylar foil positioned at the other end of the tube then generated a shock at the curved chamber entry (a 200 mm long, 30 mm  $\times$  20 mm cross-section straight channel).

Each face of the curved chamber was equipped with a 217 mm  $\times$  275 mm, 27 mm thick glass window for optical access, one in UV-silica (refraction index  $n = 1.458$ ) and the other in borosilicate-crown (N-BK7, refraction index  $n = 1.515$ ). The shock dynamics could thus be characterized via high-speed shadowgraph visualization with a Shimadzu HPV-X2 high-speed camera set at the frequency of 500 kHz and the exposure time of 200 ns. The light source was a mercury-vapour lamp. Four pressure transducers Kistler 603B (1  $\mu\text{s}$  response time, 300 kHz natural frequency, labeled  $P_1$ - $P_4$  in Fig. 1) coupled with Kistler 5018A electrostatic charge amplifiers (200 kHz bandwidth) were positioned in the tube to detect the detonation position. The average detonation velocities were defined by the ratio of the distance (250 mm) separating the transducer positions

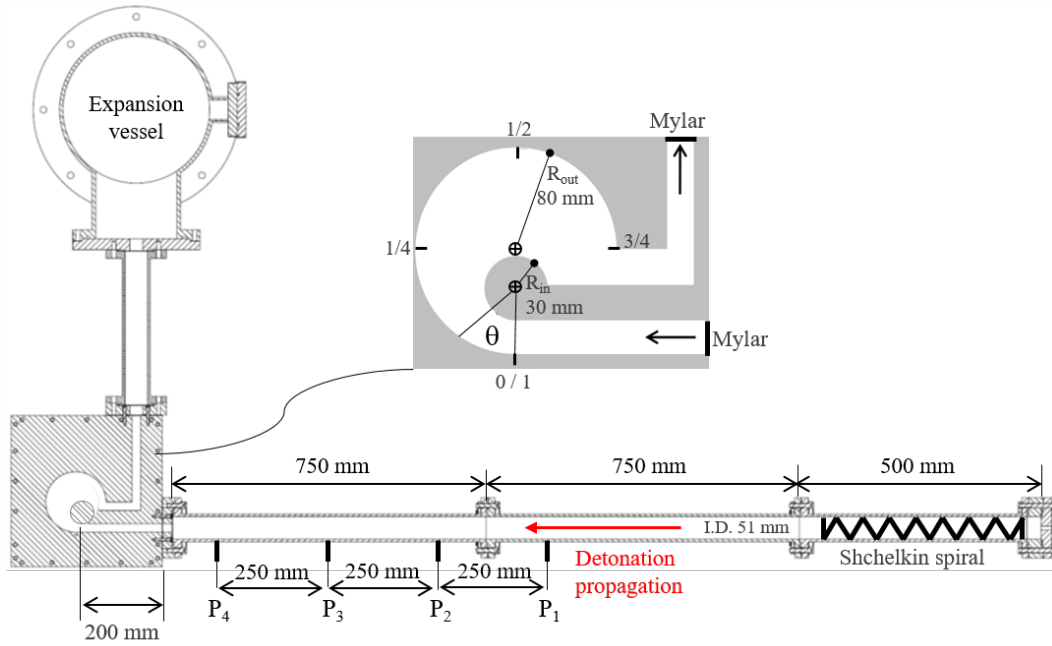


**Fig. 1** Schematic of the experimental setup. The angular positions  $\theta$  in the chamber are normalized by  $2\pi$ .

to the time intervals measured from the transducer triggering.

For all experiments, the reactive mixture in the driver tube was  $2\text{H}_2 + \text{O}_2 + 2\text{Ar}$  at the initial pressure of  $p_0 = 11$  kPa. The CEA-NASA thermochemical computer code was used to calculate the CJ equilibrium detonation velocity (1955 m/s). Its relative difference with the average velocities never exceeded  $\pm 2\%$ , so we considered that the CJ detonation regime was always achieved before the Mylar foil. The aim of the present study is to demonstrate the existence of a rotating shock regime without the support of chemical reactions. We chose the inert  $\text{He} + \text{O}_2 + 2\text{Ar}$  mixture because its thermodynamic properties are close to those of the reactive hydrogen-oxygen-argon mixture used in our previous experimental study in which we identified the steady rotating detonation regime. We chose air because its specific volume is approximately the same as that of the  $\text{He} + \text{O}_2 + 2\text{Ar}$  mixture, but not its gamma. The initial pressure  $p_{c0}$  was varied from 2 to 11 kPa for air and from 2.5 to 12 kPa for  $\text{He} + \text{O}_2 + 2\text{Ar}$ . The initial temperature was  $T_0 = 288$  K in the tube and in the chamber. We ran the experiments at least three times for each  $p_{c0}$  and inert gas.

### 3 Computational methodology

The inert flow field in the curved chamber was assumed to be inviscid and thus modelled using the Euler equations. Temperature dependent heat capacities, enthalpies

and entropies of the species and their mixtures were computed using the JANAF tables [26]. The conservation laws were solved in the two-dimensional planar geometry using the OpenFOAM Toolbox [27] and the same numerical methods and temporal and spatial discretization as those described in [21]. The fluxes at cell-faces were computed using a central-upwind Kurganov-Tadmor scheme [28, 29]. The flow variables on cell faces were reconstructed through a second-order interpolation with a symmetric van Albada flux limiter, which ensures non-oscillatory bounded transitions across shocks and contact discontinuities. The time integration used a second-order Crank-Nicolson method; the time step was dynamically adapted during the computation with an acoustic cell Courant number of 0.5 to ensure the stability of the numerical scheme. The implementation and validation of the inert part of the solver followed the same methodology as in [30]. The reactive version has shown excellent predictive capabilities for complex transients such as detonation transmission, quenching and re-initiation [21].

The computational domain reproduced the curved chamber shown in Figure 1. The conditions imposed at the chamber walls were a slip boundary for the material velocity and zero gradient for temperature, species and pressure. The same hexagonal uniform mesh (9, 286, 953 cells) as in [21] for modelling detonation transmission with a similar initial pressure range was utilized, which provided more than sufficient resolution for the inert cases at hand. The shock transmission was modeled by

propagating a detonation up the straight section of the chamber and turning off the chemistry  $35 \mu\text{s}$  later, that is,  $\sim 55 - 56 \text{ mm}$  beyond the entry, depending on the cases computed. This numerical initiation scheme mimics rather well the physical detonation/Mylar interaction because the decoupling of the reaction zone and the transmitted shock was ensured close enough beyond the interaction position (which lies outside the computational domain) and far enough ahead of the entry of the curved section (200 mm). Yet, as is discussed below (Sect. 5), the uncertainties in properly defining the initial condition may induce some quantitative discrepancies with the experimental data.

Simulations were run using 200 processors and required an average of 7,200 CPU hours for each of the cases defined in the previous section. Importantly, they were conducted based only on the knowledge of the chamber dimensions, and the initial pressures and compositions of the gases in the tube and the chamber.

## 4 Experimental results

The control parameters are the initial pressures  $p_{c0}$  and inert gas compositions in the chamber since the conditions in the detonation tube were not varied (Sect. 2).

The transmitted shocks have initially higher velocities ( $D_1$ ) and pressures ( $p_{c1}$ ) for larger initial pressure ratios ( $p_0/p_{c0}$ ) between the driver (the detonation tube) and driven sections (the chamber), that is, the lower  $p_{c0}$ , the higher  $D_1$  and the larger  $p_{c1}$ . The velocities  $D_1$  and pressures  $p_{c1}$  at the entry of the straight section of the chamber are initial conditions that combine with the dynamics of the flow field sustaining the shock to determine its dynamical behaviour in the curved section (Sect. 6). Thus, here, after the shock becomes oblique with respect to the curved outer wall,  $p_{c0}$  determines whether its reflection is of the regular or the Mach type (Sect. 1). The calculations of  $D_1$  and  $p_{c1}$  is summarized in Section 5.

The angular positions  $\theta$  are measured clockwise from the entry of the chamber curved section, in the propagation direction of the shock, and normalized by  $2\pi$  (Fig.1). Thus the shocks enter this section at  $\theta/2\pi = 0$  and exit at  $\theta/2\pi = 0.75$ . The position intervals  $[0 - 0.25]$ ,  $[0.25 - 0.5]$  and  $[0.5 - 0.75]$  are referred to below as first, second and third quadrants, respectively.

In our conditions, the Mach-type reflection was always observed, but its steadiness, stem height ( $h_{\text{Mach}}$ ) and outer-wall velocity ( $D_{\text{Mach}}$ ) depend on  $p_{c0}$ . Essentially, for each inert gas, there exists an intermediate range of  $p_{c0}$  that results in steadiness, that is, constant  $h_{\text{Mach}}$ . In this range, the larger  $p_{c0}$ , the smaller

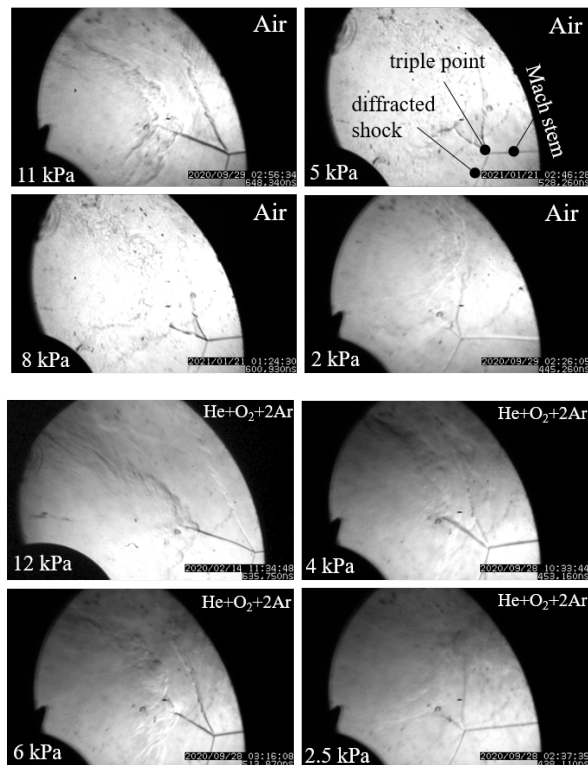


**Fig. 2** Experimental wave structures shown as shadowgraph pictures at about the same angular position in the third quadrant for air and He + O<sub>2</sub> + 2Ar.

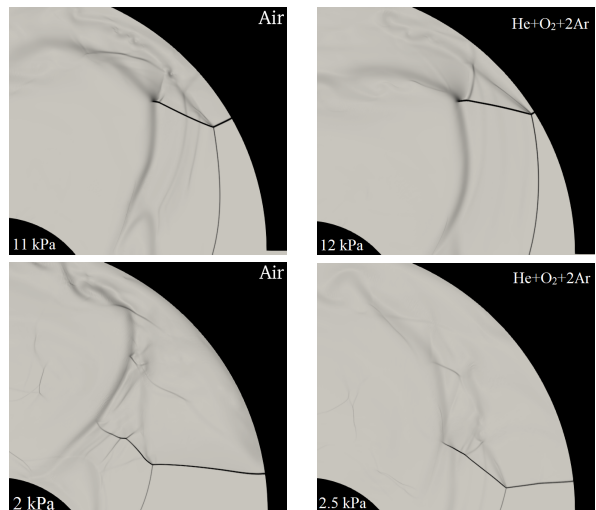


**Fig. 3** Numerical wave structures shown as shadowgraph pictures for air (left) and He + O<sub>2</sub> + 2Ar (right) at their lowest and highest initial pressures  $p_{c0}$ .

$h_{\text{Mach}}$ . Above the upper bound of the steadiness range,  $h_{\text{Mach}}$  markedly decreases during rotation, and this all the more so as  $p_{c0}$  is large. Below the lower bound,  $h_{\text{Mach}}$  slightly increases with decreasing  $p_{c0}$ . In contrast,  $D_{\text{Mach}}$  retains constant values - to within the measure-

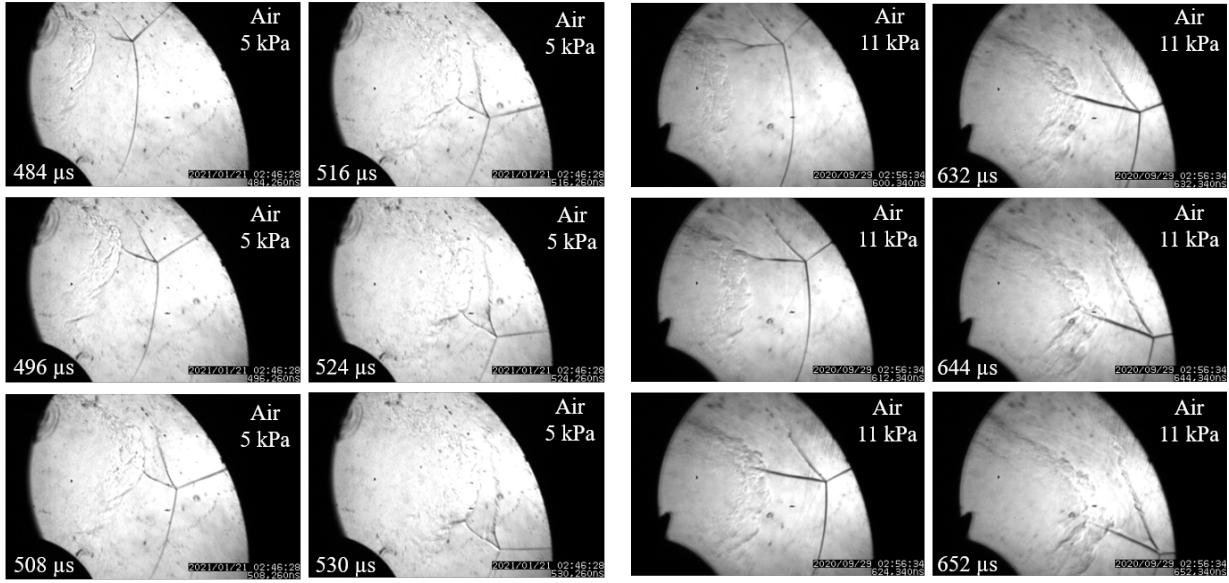


**Fig. 4** Experimental Mach stem rotation shown as a time sequence of shadowgraph pictures for air. Left:  $p_{c0} = 5$  kPa. Right:  $p_{c0} = 11$  kPa. The origin of time is taken at the entry of the straight channel.

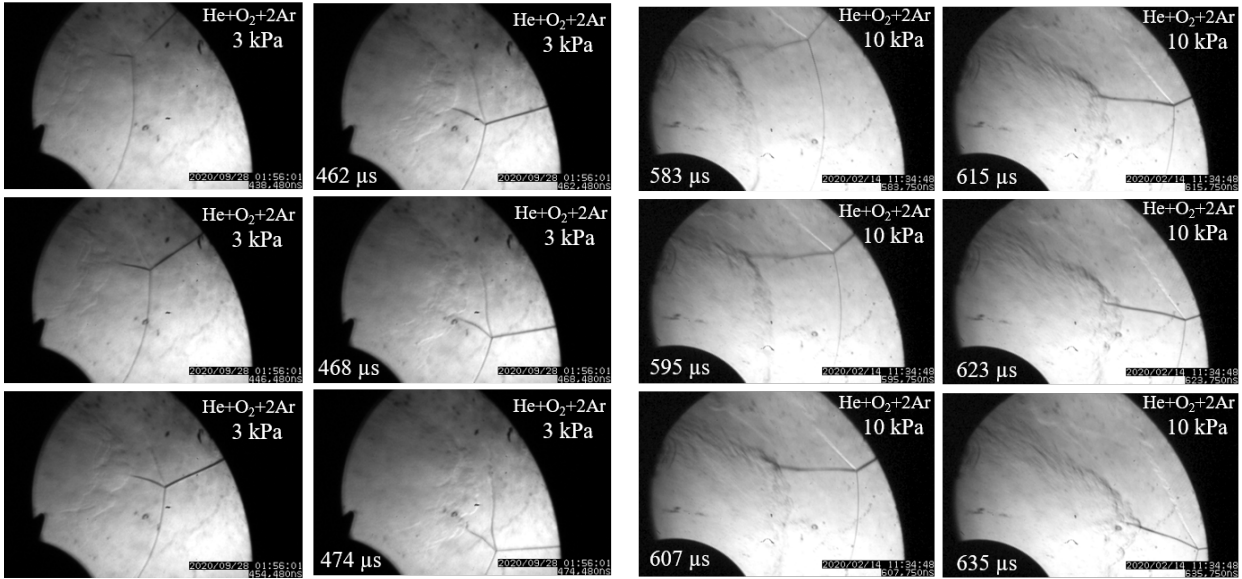


**Fig. 5** Experimental Mach stem rotation shown as a time sequence of shadowgraph pictures for He + O<sub>2</sub> + 2Ar. Left:  $p_{c0} = 3$  kPa. Right:  $p_{c0} = 10$  kPa. The origin of time is taken at the entry of the straight channel.

ment uncertainty - regardless of  $p_{c0}$ , that is, of whether the Mach configuration is steady or not. Therefore, in our conditions, the shock velocities cannot be used as a steadiness indicator. The larger velocities are obtained with the smaller  $p_{c0}$ .

Figure 2 shows excerpts from high-speed recordings at about the same angular position  $\theta/2\pi$  in the third quadrant of the chamber for air and He + O<sub>2</sub> + 2Ar. Each shows the typical Mach-type reflection, including

a Mach stem and, attached to it at some distance from the wall, two shocks and a contact discontinuity. Their comparison indicates that the stem height  $h_{\text{Mach}}$  decreases with increasing initial pressure  $p_{c0}$ ; the same is observed from the numerical wave structures shown in Figure 3.

The information on steadiness was extracted from the analyses of the high-speed recordings in the third quadrant. Typical time sequences are shown in Figure

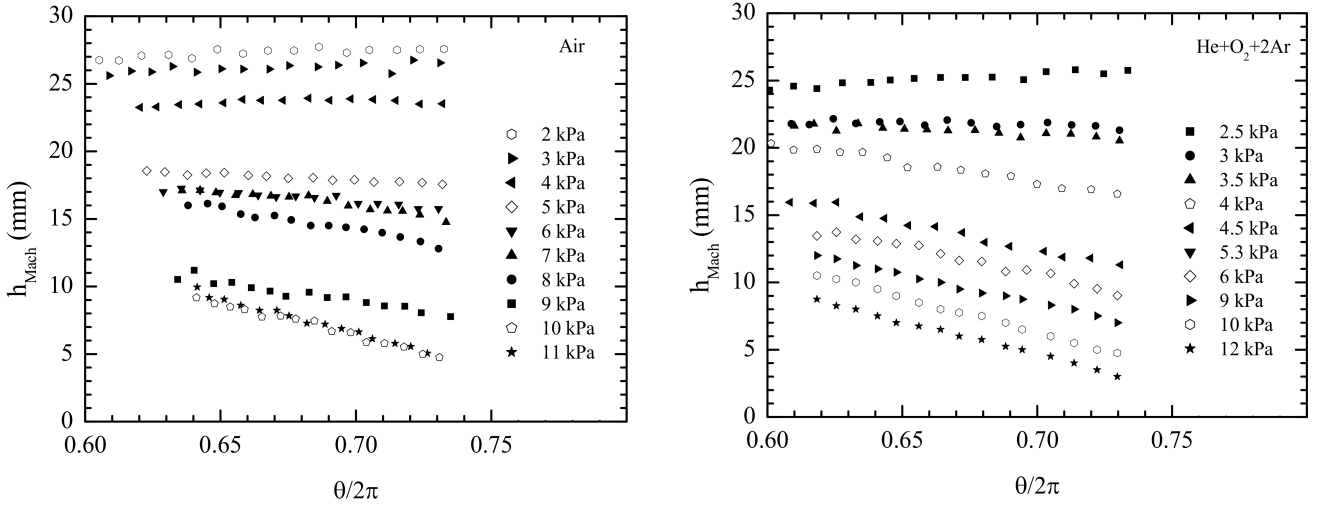


**Fig. 6** Measured Mach stem height  $h_{\text{Mach stem}}$  at outer wall as a function of the angular position  $\theta/2\pi$ . Left: air. Right: He + O<sub>2</sub> + 2 Ar.

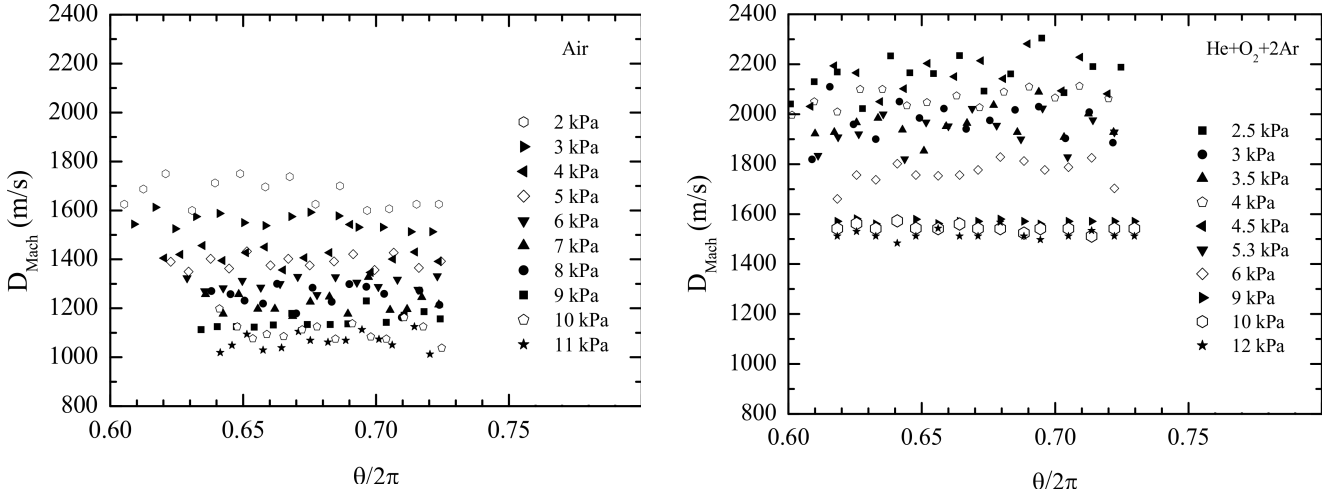


**Fig. 7** Measured Mach stem velocity  $D_{\text{Mach}}$  at outer wall as a function of the angular position  $\theta/2\pi$ . Left: air. Right: He + O<sub>2</sub> + 2 Ar.

4 for air and Figure 5 for He + O<sub>2</sub> + 2 Ar, with instants selected so that the stem positions occupy the whole angular interval  $[0.5 - 0.75]$ . The steadiness ranges were obtained by measuring the stem heights  $h_{\text{Mach}}$  and angular positions  $\theta$  for each successive image on a recording. The tangential velocities were then calculated from the outer wall radius  $R_{\text{out}} = 80$  mm and the time intervals between successive images as  $D_{\text{Mach}} = R_{\text{out}} d\theta/dt$ . These experimental values of  $h_{\text{Mach}}$  and  $D_{\text{Mach}}$  are reported in Figure 6 as a function of the normalized angular position  $\theta/2\pi$  for air and He + O<sub>2</sub> + 2 Ar. The steadiness ranges were difficult to determine precisely: their lower and upper bounds are close to each other compared to those of the investigated initial pressure  $p_{c0}$  intervals, that is,  $[3 - 5]$  kPa for air and  $[2.5 - 3.5]$

kPa for He + O<sub>2</sub> + 2 Ar (the brackets  $[$  and  $]$  at an interval left indicate inclusion and exclusion, respectively, and the contrary at an interval right).

Figure 4 shows the time sequences for air at  $p_{c0} = 5$  and 11 kPa, both values larger than the upper bound of the steadiness range. The smaller one (5 kPa), only slightly larger than the upper bound,  $h_{\text{Mach}}$  seems to be constant but a close look at Figure 6-left actually indicates a slight decrease with increasing  $\theta/2\pi$ . For the larger one (11 kPa), markedly larger than the upper bound,  $h_{\text{Mach}}$  unambiguously decreases with increasing  $\theta/2\pi$ . Figure 5 shows the time sequences for He + O<sub>2</sub> + 2 Ar at  $p_{c0} = 3$  and 10 kPa. The smaller one (3 kPa) belongs to the steadiness range, and, indeed, Fig. 6-right confirms that  $h_{\text{Mach}}$  is constant. The larger one

(10 kPa) is above the upper bound, and  $h_{\text{Mach}}$  decreases with increasing  $\theta/2\pi$ , similarly to the cases for air in Fig. 4.

The situations for which the triple point moves away from or towards the wall during rotation are referred to as direct or inverse Mach reflections, respectively [25]. For the latter case, large enough values of  $p_{c0}$  can lead to the disappearance of the Mach stem before the end of the curved section of the chamber, that is, the inverse Mach reflection turns into a regular reflection, with two shocks attached to the same point at the wall end, (e.g. Figs. 4-right and 5-right at the later instants).

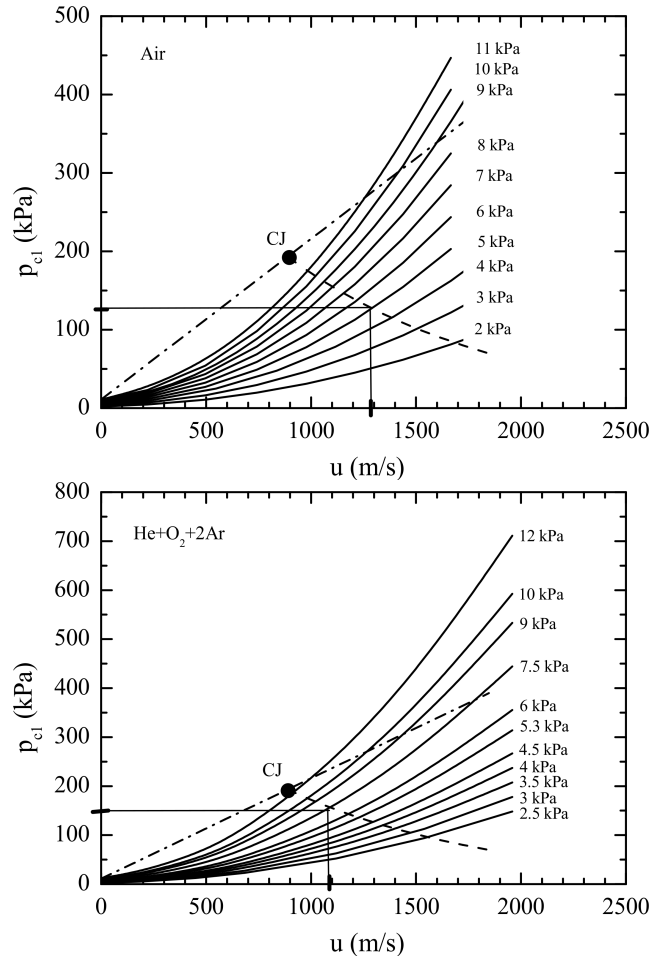
Figure 6 shows the Mach stem height  $h_{\text{Mach}}$  for air and He + O<sub>2</sub> + 2 Ar as a function of the normalized angular position  $\theta/2\pi$ . Each set bearing the same symbol on a plot corresponds to the same value of  $p_{c0}$ . In particular for air, each plot shows three clusters of data sets, that is, the gap from one cluster to another is much larger than from one data set to the other in the same cluster. We have no explanation for this non monotonic trend since the interval of  $p_{c0}$  from one data set to another is constant, 1 kPa for air and 0.5 kPa for He + O<sub>2</sub> + 2 Ar.

Figure 7 shows the Mach stem velocity  $D_{\text{Mach}}$  at the outer wall as a function of the normalized angular position  $\theta/2\pi$  for air and He + O<sub>2</sub> + 2 Ar. The data dispersion is larger than for the stem heights but seems to decrease with increasing  $p_{c0}$  at constant  $\theta/2\pi$ . As indicated above,  $D_{\text{Mach}}$  retains about constant values regardless of  $p_{c0}$ , that is, of whether the Mach configuration is steady or not. Therefore in our conditions, the velocity measurements cannot be used as a steadiness indicator. In contrast to  $h_{\text{Mach}}$ , there is no evident clusters, except for He + O<sub>2</sub> + 2 Ar at the higher three values of  $p_{c0}$  considered for which the data sets merge into one. The higher velocities are obtained with the smaller  $p_{c0}$ , consistent with the larger pressure ratios  $p_0/p_{c0}$  at the chamber entry.

## 5 Analysis

The initial shock velocities  $D_1$  at the chamber entry are used below as a reference to normalize the velocities  $D_{\text{Mach}}$  of the Mach shocks during their rotation. A similar choice was made in our previous work [20] with the same reactive gas in the tube and the chamber where the reference initial velocities were those of the CJ detonations at the chamber entry,  $D_{\text{CJ}}$  (Sects. 1 and 2). Thus an overdriven Mach rotation is characterized by normalized Mach velocities  $D_{\text{Mach}}/D_1$  greater than 1.

The velocities  $D_1$  and pressures  $p_{c1}$  are the solution to the compatibility problem expressing the continuity



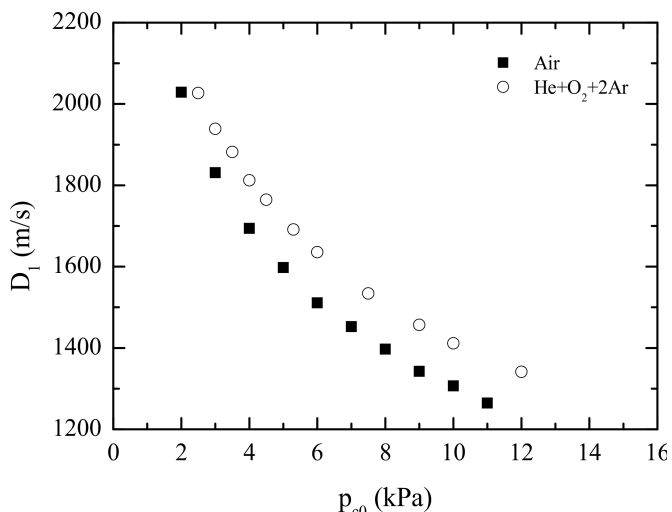
**Fig. 8** Pressure ( $p$ ) - Material velocity ( $u$ ) diagrams for air (top) and He + O<sub>2</sub> + 2 Ar (bottom). Full lines: shock polars, dashed-dotted line: Rayleigh-Michelson line of the incident CJ detonation, dashed line: expansion polar of the detonation products.

of the pressures  $p$  and the material velocities  $u$  through the material interface of the driver and driven gases (the detonation products and the shocked inert gas after impact). Indeed, this interface is a contact discontinuity. This classical calculation in compressible hydrodynamics is often taught using the shock polar technique in the  $p - u$  plane. In our conditions, the wave configuration after the detonation impact on the Mylar foil is an expansion reflected backwards in the products and a shock transmitted in the inert gas, regardless of the inert gas and its initial pressure.

The numerical tool CEA NASA [31] was used to compute the  $p - u$  shock polars for air and He + O<sub>2</sub> + 2 Ar, the CJ properties of the reactive gas, and the  $p - u$  expansion polar of its products based on a step-by-step integration procedure to determine the backwards-facing Riemann invariant. Figure 8 shows the resulting  $p - u$  diagrams. The dashed-dotted straight line is the



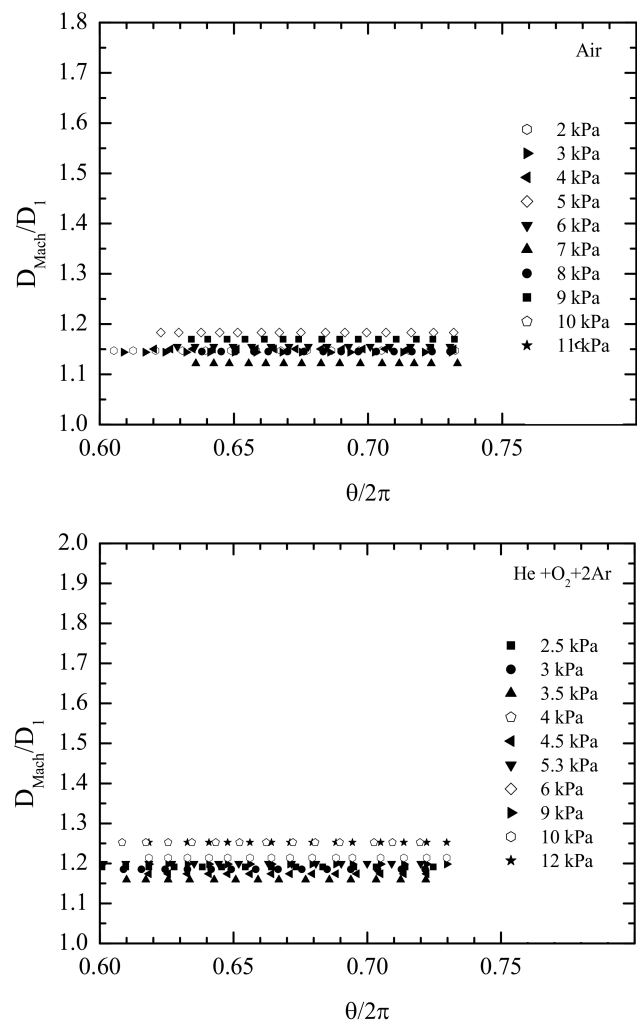
Rayleigh-Michelson (RM) line of the incident CJ detonation. The CJ point is found at the intersection of the RM line with the expansion polar of the detonation products represented by the dashed line. The full lines are the shock polars, one for each initial pressure considered in the chamber. The pressure and material velocity that ensure continuity through the interface are the coordinates of the intersection of the expansion polar and the shock polar for the considered value of  $p_{c0}$ . The corresponding shock velocity is obtained from the slope of the particular RM line that goes through this intersect, that is,  $D_1 = (p_{c1} - p_{c0})/\rho_{c0}u$ , where  $\rho_{c0}$  is the initial specific mass in the chamber. Figure 9 shows these calculated values of  $D_1$  for air and He + O<sub>2</sub> + 2 Ar as a function of  $p_{c0}$ . As expected,  $D_1$  decreases with increasing  $p_{c0}$ , and higher values are obtained with lower  $p_{c0}$ .



**Fig. 9** Shock velocities  $D_1$  at the chamber entry from shock polar analyses as a function of the initial pressure  $p_{c0}$ .

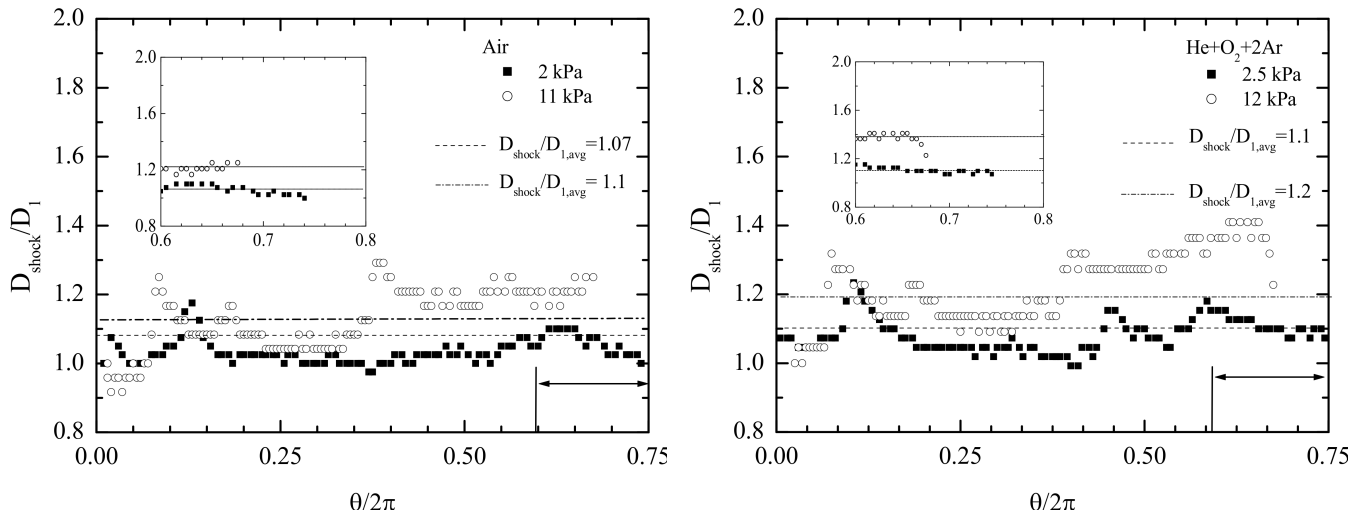
Figure 10 shows the normalized velocity ratios  $D_{\text{Mach}}/D_1$  for air and He + O<sub>2</sub> + 2 Ar as a function of the angular position  $\theta/2\pi$ . The scattered data points in the dimensional representation in Figure 7 strikingly merges into a very narrow horizontal band essentially independent of  $p_{c0}$ . This non-dimensional representation demonstrates that the values of  $D_{\text{Mach}}/D_1$  are constant and greater than 1, that is,  $1.15 \pm 0.05$  for air, and  $1.2 \pm 0.05$  for He + O<sub>2</sub> + 2 Ar. Thus, in our conditions, the Mach waves rotate with constant tangent velocities, although, as discussed above, this does not ensure the steadiness of the Mach configuration, which also requires constant heights of the Mach stems during rotation.

Figure 11 shows the tangential velocity obtained from numerical simulations at the outer wall for air



**Fig. 10** Measured Mach stem velocity  $D_{\text{Mach}}/D_1$  at outer wall for air (top) and He + O<sub>2</sub> + 2 Ar (bottom) as a function of the angular position  $\theta/2\pi$ . Values are normalized by the initial velocity  $D_1$  of the transmitted shock given by the shock polar analysis.

and He + O<sub>2</sub> + 2 Ar as a function of the angular position  $\theta/2\pi$ . The insets zoom in to the angular positions  $[0.6 - 0.75]$  where the experimental data was collected, that is, most of the third quadrant. In agreement with the experimental results, the simulated normalized values  $D_{\text{Mach}}/D_1$  for this quadrant are essentially constant and, on average, in good quantitative agreement with the experimental values. However, the diffracted shock for the largest  $p_{c0}$  overtakes the Mach stem earlier than in the experiments, as a consequence of the numerical strategy used to initialize the simulation as indicated in Section 3.



**Fig. 11** Simulated shock velocity  $D_{\text{shock}}/D_1$  at outer wall for air (left) and He + O<sub>2</sub> + 2 Ar (right) at initial pressures  $p_{c0} = 2$  and 11 kPa, and  $p_{c0} = 2.5$  and 12 kPa, respectively, as a function of the angular position  $\theta/2\pi$ . Values are normalized by initial velocity  $D_1$  of the transmitted shock given by the simulation. The experimental domain is the angular interval  $[0.6 - 0.75]$ .

## 6 Discussion and conclusion

In our previous studies [20,21], the tube and the chamber contained the same gaseous reactive mixture. In this case, we showed experimentally and numerically the possibility of the steady rotation of an overdriven Mach detonation with constant stem height along the concave outer wall of the chamber. In particular, in view of the small size of the detonation cells behind the stem and their orientation parallel to the wall, we suggested that this regime should be driven by the initial velocity of the detonation at the chamber entry and the overall geometry of the chamber. We provided additional evidence based on an implementation of Whitham's Geometrical Shock Dynamics (GSD) [22], with detonation waves modelled as fully-reactive discontinuities [23]. In our conditions, a detonation at the chamber entry could be viewed as a CJ discontinuity, whose velocity is determined essentially by the heat of reaction of the reactive mixture for the considered initial state. That eliminated the dependence of the wave dynamics on chemical kinetics, and still, this simple modelling could generate a steadily rotating overdriven Mach detonation.

These observations motivated the present study, in which the chamber was filled with inert gases. The shocks were generated from a shock-tube device driven by the expanding products of a detonation in the tube, and their initial velocities, at the chamber entry, were calculated through the shock polar technique. Our experimental recordings and numerical simulations both produced steadily rotating Mach shocks with constant stem height and tangential velocities at the chamber wall higher than their initial values at the chamber en-

try. However, the steadiness parametric ranges, that is, 2 kPa for air and 1 kPa for He + O<sub>2</sub> + Ar were found narrower than the 4 kPa reported for the reactive cases in [20,21].

An interpretation could be that steadiness in the inert case is only an appearance, that is, a non-detectable direct or inverse Mach reflection, with the triple point moving very slowly away from or towards the wall and not rotating parallel to it. Actually, each point in Figure 6 results from averaging data collected from at least three shots, i.e., with each initial pressure  $p_{c0}$  investigated three times. The stem heights  $h_{\text{Mach}}$  were obtained through software processing with resulting accuracy better than 0.5 mm (2 pixels, 1/4 mm each), which is much smaller than the fluctuations of  $h_{\text{Mach}}$  for the values of  $p_{c0}$  defining the steadiness ranges. Furthermore, the accuracy on  $p_{c0}$  is less than 0.1 kPa, which is much smaller than the magnitudes of  $p_{c0}$  and the steadiness interval. Thus, we retained the other interpretation, namely the steady rotation of a constant-height Mach stem.

That raises the question of why the steadiness ranges for the inert cases are narrower than for the reactive case although the velocity ratios are close to each other. Both cases involve the same apparent characteristic lengths and velocities, namely the Mach stem height  $h_{\text{Mach}}$ , the chamber outer radius  $R_{\text{out}}$ , and the discontinuity velocity at the chamber entry  $D_1$ . We suggest that the flow field behind the discontinuity is a likely possibility for distinguishing one case from the other. For the reactive case, the initial condition is the CJ regime. Its flow field is described by the self-similar solution of

Taylor-Zel'dovich [32], which includes the self-sustained CJ state. The wall concavity then acts as a converging channel which adds the overdrive effect, as pointed out in our GSD modeling [22, 23]. The rotating Mach shock does not benefit from an initially self-sustained flow, and, therefore, is more difficult to install due to the permanent influence of the back flow on the subsonic Mach shock.

Thus the regimes of steady rotation of Mach detonations and shocks are driven by the chamber geometry, but the flow field behind the discontinuity appears to influence their parametric range of observation. A non-dimensional formulation of the problem based on characteristic lengths that would take into account the physical control parameters and the flow field does not appear evident, so further investigations of these regimes should rely only on specific experiments supported by high-resolution numerical simulations. In our view, further analysis should look at the effect of the chamber dimensions, namely its outer radius and cross-section area. For example, the investigations could consider determining the lower and upper outer radii for observing the Mach stem regime.

**Acknowledgements** The authors would like to thank Alain Claverie, CNRS Research Engineer, for his technical assistance. The computations were carried out on the supercomputer facilities of the *Mésocentre de Calcul de Poitou Charentes*. This work was supported by the CPER-FEDER Project of *Région Nouvelle Aquitaine* and is part of the French government program *Investissements d'Avenir* (EUR INTREE ANR-18-EURE-0010).

## Declarations

Ethical approval

Not applicable

Competing interests

No competing interests

Authors' contributions

All authors whose names appear on the submission

1) made substantial contributions to the conception or design of the work, the acquisition, analysis and, interpretation of data.

2) drafted the work and revised it critically for important intellectual content.

3) approved the version to be published; and

4) agree to be accountable for all aspects of the work in ensuring that questions related to the accuracy or integrity of any part of the work are appropriately investigated and resolved.

Funding

Not applicable

Availability of data and materials

The data that support the findings of this study are available from the corresponding author upon reasonable request.

## References

1. G Canteins. *Etude de la détonation continue rotative : application à la propulsion (Thèse de doctorat)*. Université de Poitiers, 2006.
2. S.M. Frolov, V.S. Aksenov, V.S. Ivanov, and I.O. Shamshin. Large-scale hydrogen-air continuous detonation combustor. *Int. J. Hydrog. Energy*, 40(3):1616–1623, 2015.
3. J.A. Nicholls, R.E. Cullen, and K.W. Ragland. Feasibility studies of a rotating detonation wave rocket motor. *J. Spacecr.*, 3(6), 1966.
4. P. Wolanski. RDE research and development in Poland. *Shock Waves*, 31:623–636, 2021.
5. X. Tang, J. Wang, and Y. Shao. Three-dimensional numerical investigations of the rotating detonation engine with a hollow combustor. *Combustion and Flame*, 162(4):997–1008, 2015.
6. V. Anand, A.C.S. George, and E.J. Gutmark. Hollow rotating detonation combustor. *Proceedings of the 54<sup>th</sup> AIAA Aerospace Sciences Meeting (Reston, Virginia)*, pages 1–15, 2016.
7. F.A. Bykovskii and E.F. Vedernikov. Continuous detonation combustion of an annular gas-mixture layer. *Combust. Explos. Shock Waves*, 32(5):489–491, 1996.
8. W. Lin, J. Zhou, S. Liu, and Z. Lin. An experimental study on  $CH_4/O_2$  continuously rotating detonation wave in a hollow combustion chamber. *Experimental Thermal and Fluid Science*, 62:122–130, 2015.
9. H. Zhang, W. Liu, and S. Liu. Experimental investigations on  $H_2/air$  rotating detonation wave in the hollow chamber with Laval nozzle. *International Journal of Hydrogen Energy*, 42(5):3363–3370, 2017.
10. S. Hansmetzger, R. Zitoun, and P. Vidal. A study of continuous rotation modes of detonation in an annular chamber with constant or increasing section. *Shock Waves*, 28(5):1065–1078, 2018.
11. D.H. Edwards, P. Fearnley, G.O. Thomas, and M.A. Nettleton. Shocks and detonation in channels with 90° bends. *Proceedings of the First Int. Specialist Meeting on Combustion (Talence, France)*, pages 431–435, 1981.
12. S.M. Frolov, V.S. Aksenov, and I.O. Shamshin. Shock wave and detonation propagation through U-bend tubes. *Proceedings of the Combustion Institute*, 31(2):2421–2428, 2007.
13. Y. Kudo, J. Nagura, J. Kasahara, Y. Sasamoto, and A. Matsuo. Oblique detonation waves stabilized in rectangular-cross-section bent tubes. *Proceedings of the Combustion Institute*, 2(33):2319–2326, 2011.
14. H. Nakayama, T. Moriya, J. Kasahara, A. Matsuo, Y. Sasamoto, and I. Funaki. Stable detonation wave propagation in rectangular-cross-section curved channel. *Combustion and Flame*, 2(159):859–869, 2012.
15. H. Nakayama, J. Kasahara, A. Matsuo, and I. Funaki. Front shock behavior of stable curved detonation waves in rectangular-cross-section curved channel. *Proceedings of the Combustion Institute*, 34(2):1936–1947, 2013.

16. Y. Sugiyama, Y. Nakayama, A. Matsuo, H. Nakayama, and J. Kasahara. Numerical investigations on detonation propagation in a two-dimensional curved channel. *Combustion Science and Technology*, 186(1):1662–1679, 2014.
17. M. Short, J. Quirk, C. Meyer, and C. Chiquete. Steady detonation propagation in a circular arc: a detonation shock dynamics model. *Journal of Fluid Mechanics*, 807:87–134, 2016.
18. M. Short, J. Quirk, C. Chiquete, and Meyer S.D. Detonation propagation in a circular arc: reactive burn modelling. *Journal of Fluid Mechanics*, 835:970, 2018.
19. M. Short, C. Chiquete, and J Quirk. Propagation of a stable gaseous detonation in a circular arc configuration. *Proceedings of the Combustion Institute*, 37(3):3593–3600, 2019.
20. V. Rodriguez, C. Jourdain, P. Vidal, and R. Zitoun. An experimental evidence of steadily-rotating overdriven detonation. *Combustion and Flame*, 202(1):132–142, 2019.
21. J. Melguizo-Gavilanes, V. Rodriguez, P. Vidal, and Zitoun R. Dynamics of detonation transmission and propagation in a curved chamber: a numerical and experimental analysis. *Combustion and Flame*, 223:460–473, 2021.
22. G.B. Whitham. *Linear and nonlinear waves*. John Wiley and sons, 1974.
23. C. Jourdain, V. Rodriguez, P. Vidal, and R. Zitoun. Steadily-rotating overdriven detonation: comparison of experiments with geometrical shock dynamics modeling. In *AIAA Scitech 2019 Forum*, page 0200, San Diego, CA, 2019.
24. H. Hornung. Regular and Mach reflection of shock waves. *Annual Review of Fluid Mechanics*, 18(1):33–58, 1986.
25. G. Ben-Dor. *Shock wave reflection phenomena*. Springer Science, 1992.
26. A. Burcat, B. Ruscic, et al. Third millenium ideal gas and condensed phase thermochemical database for combustion (with update from active thermochemical tables). Technical report, Argonne National Lab.(ANL), Argonne, IL (United States), 2005.
27. H.G. Weller, G. Tabor, H. Jasak, and C. Fureby. A tensorial approach to computational continuum mechanics using object-oriented techniques. *Comput. Phys.*, 12:620–631, 1998.
28. A. Kurganov and E. Tadmor. New high-resolution central schemes for nonlinear conservation laws and convection–diffusion equations. *Journal of Computational Physics*, 160(1):241–282, 2000.
29. A. Kurganov, S. Noelle, and G. Petrova. Semidiscrete central-upwind schemes for hyperbolic conservation laws and Hamilton–Jacobi equations. *SIAM Journal on Scientific Computing*, 23(3):707–740, 2001.
30. M. Kraposhin, A. Bovtrikova, and S. Strijhak. Adaptation of Kurganov-Tadmor numerical scheme for applying in combination with the PISO method in numerical simulation of flows in a wide range of Mach numbers. *Procedia Computer Science*, 66:43–52, 2015.
31. S. Gordon and B. McBride. Computer program for calculation of complex chemical equilibrium compositions and applications, i. analysis, (ref. 1311), tech. rep. <https://cearun.grc.nasa.gov/>, 1994.
32. G.I. Taylor. The dynamics of the combustion products behind plane and spherical detonation fronts in explosives. *Proc. Roy. Soc. A*, 200:235–247, 1950.